A Generalized Wavefront-Curvature-Corrected Polar Format Algorithm to Focus Bistatic SAR Under Complicated Flight Paths

Yuxuan Miao, *Student Member, IEEE*, Junjie Wu, *Member, IEEE*, Zhongyu Li, *Member, IEEE*, and Jianyu Yang, *Member, IEEE*

***Abstract*—Bistatic synthetic aperture radar (BiSAR) imaging is faced with two major challenges: large scene imaging and adaptability to unideal platform motion in practice. In order to deal with these two problems, a generalized wavefront-curvature-corrected polar format algorithm (PFA) is proposed in this article. The traditional PFA is little restricted on geometry configuration and platform motion, but its application to large scene imaging is limited by the far-field planar wavefront assumption. To solve this limitation, this article derives the phase error caused by wavefront curvature and analyzes its influence on both geometric distortion and defocusing effect in detail. Based on the analysis, we present a wavefront curvature completely correcting method through space-variant phase compensation using the analytical wavefront curvature phase in wavenumber-domain, which is derived through method of series reversion. What's more, an efficient realization of the space-variant phase compensation based on two-stage image division is given to avoid high overlap rate in the traditional image division method. The proposed method can obtain well focused and geometric undistorted image for BiSAR under complicated flight paths, and it also keeps the logarithmic complexity of traditional PFA. The effectiveness of the proposed method is verified by numerical simulations.**

***Index Terms*—Bistatic SAR (BISAR), complicated flight paths, large scene, polar format algorithm (PFA), unideal motion, wavefront curvature.**

I. Introduction

BISTATIC synthetic aperture radar (BiSAR) has the unique advantage of flexible imaging geometry configuration, thus it can be applied to earth remote sensing and reconnaissance in various application modes such as forward-looking, spotlight or strip-map, etc. Due to the application prospect, BiSAR has attracted more and more researchers around the world to carry out works in these years. Nowadays, BiSAR imaging techniques are becoming mature as more and more airborne and spaceborne experiments have been carried out [1]–[5] and literatures on signal processing algorithms have been published [6]–[10]. As one of the most important application, There are already some literatures about forward-looking mode on its theory and prospect [11], [12] and some results on its imaging processing in some specific configurations [13]–[17].

However, when applying BiSAR to applications with complicated geometries, the 2-D space-variance of echo signal makes it difficult to obtain well-focused large scene image, especially in forward-looking mode where the nonlinearity of space-variation gets more significant. What's more, the platform trajectories are usually unideal in practice. Under complicated flight paths, there are few imaging methods that can be well applicable, except for some point-by-point-based methods like back-projection algorithm (BPA) that suffer from high computational complexity. Generally speaking, the problems of large-scene imaging and adapting to complicated flight paths are relevant. Defocusing effect in large-scene imaging is mainly caused by quadratic component of the phase error with respect to azimuth time induced by space-variance. Higher-order trajectories may result in higher quadratic phase error (QPE) compared to cases with linear trajectories, which greatly reduces the valid imaging scene-size for traditional imaging algorithms. Methods with both efficiency and adaptability to complicated flight paths are needed to be researched.

Currently, there are mainly two types of SAR imaging algorithms: time-domain projection algorithms represented by BPA and frequency-domain algorithms mainly including Range-Doppler Algorithm (RDA), Omega-K Algorithm and Chirp-scaling Algorithm (CSA). Time-domain projection algorithms like BPA are ideal in focusing SAR images, but its computational cost is too large as mentioned above with cubic complexity. Frequency-domain algorithms are usually computationally efficient with logarithmic complexity, but there are few methods that can deal with 2-D space-variation. Some methods based on omega-K or chirp-scaling are proposed to solve this problem in some specific geometric configurations [7], [9], but they are limited in terms of modes and platform motion.

The difficulties in processing BiSAR data for those frequency domain algorithms like RDA, CSA, and Omega-KA can be concluded as the following two aspects. On one hand, these

Manuscript received May 29, 2019; revised April 6, 2020; accepted May 6, 2020. Date of publication June 4, 2020; date of current version July 8, 2020. This work was supported in part by the National Natural Science Foundation of China under Grant 61922023, Grant 61771113, and Grant 61801099, in part by the Fundamental Research Funds for Central Universities under Grant 2672018ZYGX2018J017, and in part by the Postdoctoral Innovation Talent Support Program. *(Corresponding author: Junjie Wu.)*

The authors are with the School of Information and Communication Engineering, University of Electronic Science and Technology of China, Chengdu 611731, China (e-mail: yuxuanm_work@126.com; junjie_wu@uestc.edu.cn; zhongyu_li@hotmail.com; jyyang@uestc.edu.cn).

Digital Object Identifier 10.1109/JSTARS.2020.2999966

algorithms usually require analytical point target reference spectrum (PTRS), whose derivation is not easy due to the double square roots in the range history. Though some results are presented for some relatively ideal cases [18]–[22], this problem is rather significant in cases with complicated flight paths. On the other hand, algorithms based on the analytical PTRS is hard to deal with the 2-D space-variation of echo signal, as is discussed above. Actually, these problems mainly come from processing in azimuth frequency domain (also called Doppler domain). Because the platform trajectories are in azimuth time domain, algorithms in this domain like BPA usually have strong adaptability to various platform motion.

As another important imaging method, polar format algorithm (PFA) is widely used in spotlight SAR. Different from traditional frequency domain imaging methods, this algorithm multiplies the echo signal by the reference function in azimuth time and range frequency domain, thus it can well adapt to BiSAR with various geometries (including forward-looking) and even with complicated flight paths in the same way as BPA. What's more, its computational complexity is as low as Omega-KA. However, this algorithm is based on a far-field planar wavefront assumption, which greatly restricts its valid imaging scene size. Polar format imaging for BiSAR is first analyzed in [23]. Correction for wavefront curvature is researched in several literatures [24]–[27], but they all have different limitations thus are unable to solve the problems well in BiSAR with complicated platform motion.

In this article, we propose a generalized wavefront-curvature-corrected PFA that is applicable for BiSAR with complicated platform motion. The trajectories of both the receiver and the transmitter are assumed to be high-order polynomials of azimuth time. Original PFA under planar wavefront assumption for BiSAR is first reviewed. In order to deal with the problem of wavefront curvature, we derive the high-order approximated expression of the curvature error and analyze its influence on the final image through its Taylor expansions to obtain some necessary results. Based on the curvature error analysis, we derive the phase compensation filter in wavenumber domain for wavefront curvature correction through series reversion. To efficiently realize the space-variant compensation, a two-stage image division method is presented to reduce the high overlap rate in the traditional image division method. Since completely correcting the wavefront curvature error, the proposed method can obtain well-focused and geometric undistorted image for BiSAR under arbitrary finite-order platform trajectories.

The rest of this article is organized as follows. Section II defines the imaging geometry and builds the signal model. Original PFA for BiSAR is reviewed in Section III. Section IV derives and analyzes the influence of wavefront curvature error. Section V presents the wavefront curvature correction method. Numerical simulations are given in Section VI to verify the proposed results. Section VII concludes this article.

II. Signal Model

A. Geometry Definition

Fig. 1 illustrates the imaging geometry of BiSAR with a general configuration. Both the receiver and the transmitter work in spotlight mode, and their beam centers point at the scene center O. The receiver that usually works in squint or forward-looking mode flies with a trajectory which can be arbitrary with a finite order. The transmitter works in squint or side-looking mode and also flies with a finite-order trajectory.

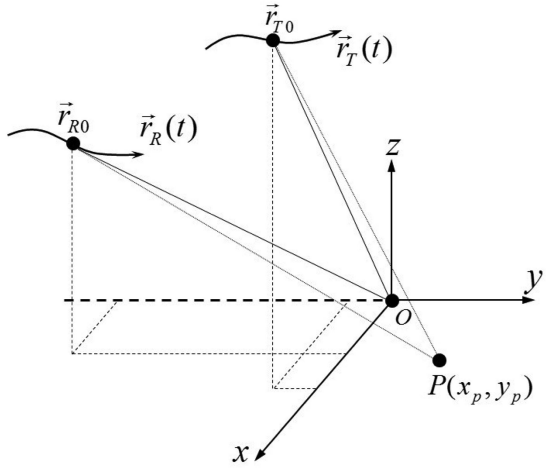

Fig. 1. Imaging geometry definition.

The trajectories of the two platforms are defined as $\vec{r}_R(t)$ and $\vec{r}_T(t)$, respectively, which are both within one synthetic aperture time and are given by

$$\vec{r}_T(t) = [x_T(t), y_T(t), z_T(t)] \tag{1a}$$

$$\vec{r}_R(t) = [x_R(t), y_R(t), z_R(t)]\,. \tag{1b}$$

B. SAR Signal Model

Suppose the transmitted signals are linear frequency modulated pulses, for the point target $P(x_p, y_p)$ in Fig. 1, the received baseband signal can be written as

$$\begin{aligned} s_r(\tau, t; x_p, y_p) = {} & w_r\left[\tau - \frac{R_p(t; x_p, y_p)}{c}\right] w_a\left(\frac{t}{T_a}\right) \\ & \times \exp\left[-j2\pi\frac{R_p(t; x_p, y_p)}{\lambda}\right] \\ & \times \exp\left\{j\pi K_r\left[\tau - \frac{R_p(t; x_p, y_p)}{c}\right]^2\right\} \end{aligned} \tag{2}$$

where w_r is the range envelope and w_a is the azimuth envelope. T_a is the synthetic aperture time. K_r represents the FM rate of the transmitted signal. c is the speed of light and λ represents the wavelength of the carrier. $R_p(t; x_p, y_p)$ is the Bistatic slant range history of target P, which is given by

$$\begin{aligned} R_p(t; x_p, y_p) = {} & \|\vec{r}_T(t) - [x_p, y_p, 0]\|_2 \\ & + \|\vec{r}_R(t) - [x_p, y_p, 0]\|_2. \end{aligned} \tag{3}$$

After range Fourier transformation and range matched filtering, the signal becomes

$$\begin{aligned} S_r(f_\tau, t; x_p, y_p) = {} & W_r(f_\tau)\, w_a\left(\frac{t}{T_a}\right) \\ & \exp\left[-j2\pi\frac{f_c + f_\tau}{c} R_p(t; x_p, y_p)\right] \end{aligned} \tag{4}$$

where W_r is the frequency-domain envelope corresponding to w_r, f_τ represents the range frequency and f_c is the carrier frequency.

III. PFA for BiSAR

In this algorithm, the first step is to make the azimuth dechirp (also known as the bulk compression) for the signal given by (4) using the reference function of the scene center O,

$$\begin{aligned} S_d(f_\tau, t; x_p, y_p) &= S_r(f_\tau, t; x_p, y_p) \times {S_r}^*(f_\tau, t; 0, 0) \\ &= \exp\left[-j2\pi \frac{f_c + f_\tau}{c} \Delta R_p(t; x_p, y_p)\right] \end{aligned} \tag{5}$$

where the envelop functions are omitted and

$$\begin{aligned} \Delta R_p(t; x_p, y_p) &= \|\vec{r}_T(t) - [x_p, y_p, 0]\|_2 - \|\vec{r}_T(t)\|_2 \\ &+ \|\vec{r}_R(t) - [x_p, y_p, 0]\|_2 - \|\vec{r}_R(t)\|_2 \end{aligned} \tag{6}$$

which is called the differential distance.

Under the planar wavefront assumption, the differential distances of both the receiver and the transmitter are approximated as only linear with respect to x_p and y_p, which are denoted by $\Delta\hat{R}_R(t; x_p, y_p)$ and $\Delta\hat{R}_T(t; x_p, y_p)$. That is

$$\Delta\hat{R}_R(t; x_p, y_p) = -\frac{x_R(t)x_p}{R_R(t)} - \frac{y_R(t)y_p}{R_R(t)} \tag{7a}$$

$$\Delta\hat{R}_T(t; x_p, y_p) = -\frac{x_T(t)x_p}{R_T(t)} - \frac{y_T(t)y_p}{R_T(t)} \tag{7b}$$

where

$$R_R(t) = \|\vec{r}_R(t)\|_2 \tag{8a}$$

$$R_T(t) = \|\vec{r}_T(t)\|_2. \tag{8b}$$

Thus, the approximated total differential distance is given by

$$\begin{aligned} \Delta\hat{R}_p(t; x_p, y_p) = &-\left[\frac{x_T(t)}{R_T(t)} + \frac{x_R(t)}{R_R(t)}\right] x_p \\ &- \left[\frac{y_R(t)}{R_R(t)} + \frac{y_T(t)}{R_T(t)}\right] y_p. \end{aligned} \tag{9}$$

Then, the actual phase of S_d in (5) can be expressed as

$$\begin{aligned} &\varphi_p(f_\tau, t; x_p, y_p) \\ &= -2\pi \frac{f_c + f_\tau}{c} \left[\Delta\hat{R}_p(t; x_p, y_p) + \Delta R_{\text{cur}}(t; x_p, y_p)\right] \\ &= \hat{\varphi}(f_\tau, t) + \varphi_{\text{cur}}(f_\tau, t) \end{aligned} \tag{10}$$

where ΔR_{cur} denotes the range error caused by wavefront curvature. $\hat{\varphi}$ denotes the approximated differential phase corresponding to $\Delta\hat{R}_p$ and φ_{cur} represents the ignored wavefront curvature phase corresponding to ΔR_{cur}.

Note that $\hat{\varphi}$ and φ_{cur} are also functions of x_p, y_p, which are omitted here for convenience.

Based on the expressions above, transform S_d into 2-D wavenumber domain according to the following mapping:

$$k_x = k_r \left[\frac{x_T(t)}{R_T(t)} + \frac{x_R(t)}{R_R(t)}\right] \tag{11a}$$

$$k_y = k_r \left[\frac{y_T(t)}{R_T(t)} + \frac{y_R(t)}{R_R(t)}\right] \tag{11b}$$

which is called the polar format mapping. k_x and k_y denote the wavenumbers in x and y directions, respectively, and

$$k_r = \frac{2\pi}{c}(f_c + f_\tau) \tag{12}$$

which denotes the wavenumber in range direction.

Then, S_d becomes

$$\begin{aligned} &H_p(k_x, k_y; x_p, y_p) \\ &= \exp\left\{j\left[k_x x_p + k_y y_p + \varphi_{\text{cur}}(k_x, k_y; x_p, y_p)\right]\right\} \end{aligned} \tag{13}$$

where $\varphi_{\text{cur}}(k_x, k_y; x_p, y_p)$ is the wavenumber-domain curvature phase error transformed from $\varphi_{\text{cur}}(f_\tau, t)$.

The polar format mapping can be realized through a 2-D interpolation to make (13) uniformly sampled with respect to k_x and k_y, then the final image can be obtained through a 2-D IFFT. We can simply realize the mapping through nearest-neighbor interpolation, whose accuracy can be improved by upsamping the data before performing the mapping.

IV. Wavefront Curvature Error Analysis

For BiSAR, PFA can work well in small scene size imaging with respect to the focusing effect despite slight geometric distortion. However in large scene size imaging, the planar wavefront assumption is no more accurate. The wavefront curvature error may result in severe defocusing effect and also geometric distortion. Therefore, methods of curvature error correction are needed. Before presenting the correction method, we first analyze the curvature error to obtain some necessary results.

The curvature error lies in the difference between ΔR_p in (6) and $\Delta\hat{R}_p$ in (9). That is

$$\Delta R_{\text{cur}}(t; x_p, y_p) = \Delta R_p(t; x_p, y_p) - \Delta\hat{R}_p(t; x_p, y_p). \tag{14}$$

When the distance between P and O is not so large compared with the operating distances of the radar platforms, high-order terms of (14) with respect to x_p, y_p can be ignored. Considering the practical conditions, we retain its expansion terms up to third order as

$$\begin{aligned} &\Delta R_{\text{cur}}(t; x_p, y_p) \\ &\approx \Delta\hat{R}_{\text{cur}}(t; x_p, y_p) \\ &= \sum_{i+j=2}^{i,j\in N} \frac{C_2^i \partial^2 \Delta R_{\text{cur}}(t; x_p, y_p)}{2\partial x_p^i \partial y_p^j} x_p^i y_p^j \\ &\quad + \sum_{i+j=3}^{i,j\in N} \frac{C_3^i \partial^3 \Delta R_{\text{cur}}(t; x_p, y_p)}{6\partial x_p^i \partial {y_p}^j} x_p^i y_p^j. \end{aligned} \tag{15}$$

Since the trajectories are assumed as high order, this curvature range error, which produces a corresponding phase error, also contains several orders Taylor components with respect to t. As is indicated in [28], the zeroth- and first-order components result in position shift in range direction and azimuth direction, respectively, the second-order component mainly impacts the

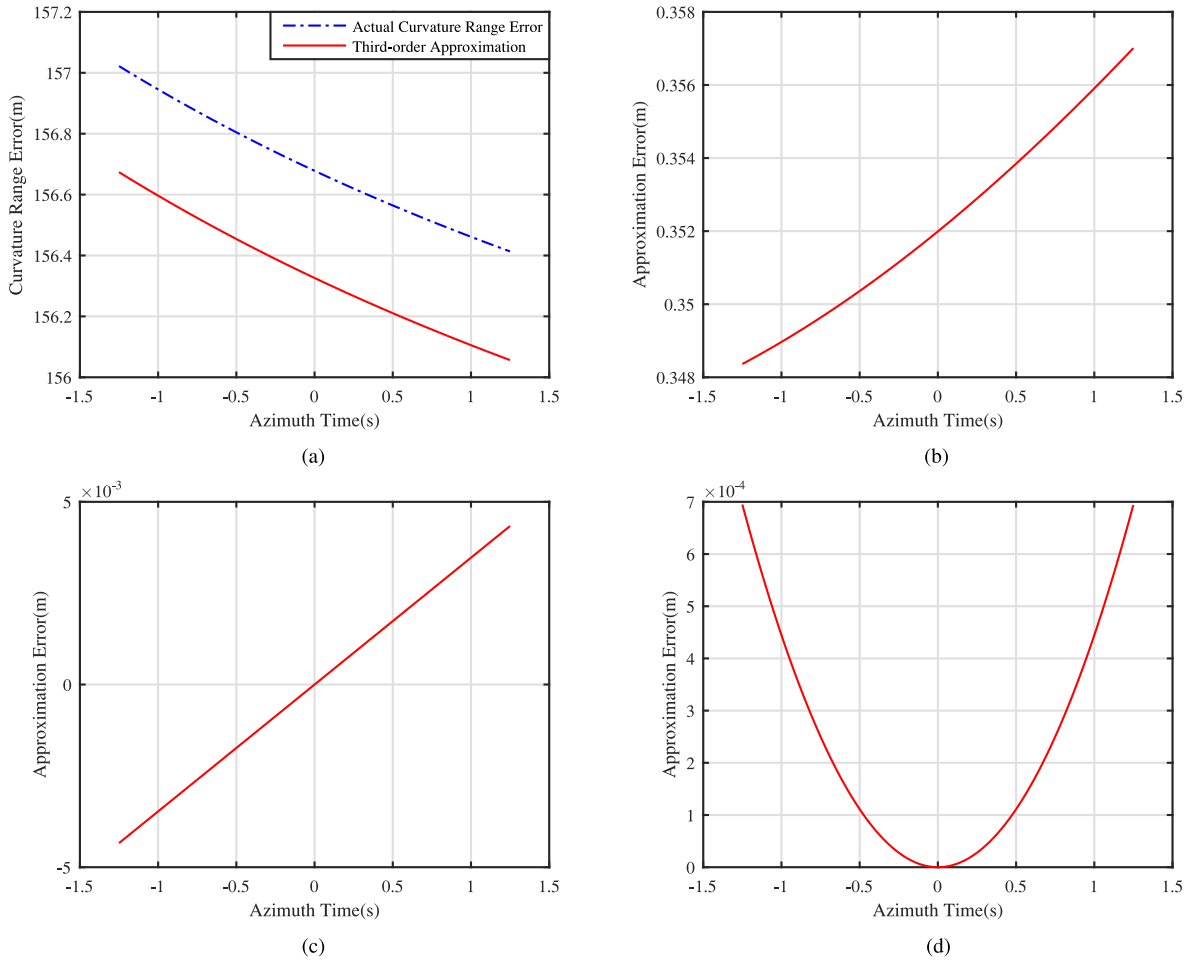

Fig. 2. Approximation of the curvature range error. (a) Actual curvature range error and its third-order approximation. (b) The approximation error. (c) First-order component of the approximation error. (d) The second-order component of the approximation error.

focusing effect and high order ones may cause asymmetric sidelobes. The following analysis is carried out based on these classic conclusions.

Fig. 2 shows the residual error of this third-order approximation at a position $(1200, 1200)$ m for a certain geometry (the specific parameters are presented in Section V). Though the total approximation error is up to 0.35 m, but it mainly consists of zero- and first-order terms with respect to t while the second-order component that is no more than 7×10^{-4} m is small enough compared with the 0.03 m wavelength. The zeroth- and first-order components will induce residual positioning errors with same orders of magnitude when this approximation is used for the subsequent processing. Since they are nevertheless very small, this approximation is accurate enough for imaging in a 2400×2400 m area.

When the imaging area gets even larger, the accuracy of this third-order model will get worse. This will be discussed in Section V.

Next, we come to the influence of the curvature range error. Notice that the curvature range error directly induces a phase error in range-frequency azimuth-time domain, which is defined as the curvature phase $\varphi_{\text{cur}}(f_\tau, t)$. As is already indicated, the zeroth- and first-order components may result in geometric distortion while the second-order one affects focusing effect. These influences are discussed in [29], but since we are aiming at solving the imaging problems for complicated platform motion, it is necessary to make derivations and analysis renewedly.

A. *Geometric Distortion and Distorted Coordinate Mapping*

Position errors in range and azimuth directions caused by the zeroth- and first-order components of the curvature phase may result in geometric distortion due to the space-variation of the error. Generally, a rectangular area will turn out to be a curved-edge shape in a PFA image. This phenomenon can be seen in Fig. 3.

For traditional algorithms, a position error caused by the phase error can be computed directly through the zeroth- and the first-order Taylor terms, which correspond to center slant range and Doppler centroid, respectively. However, for PFA, the final image is obtained after the polar format mapping, thus the position error is different from that of traditional algorithms. In order to obtain the expression of distorted coordinates for BiSAR PFA, we carry out inference as follows.

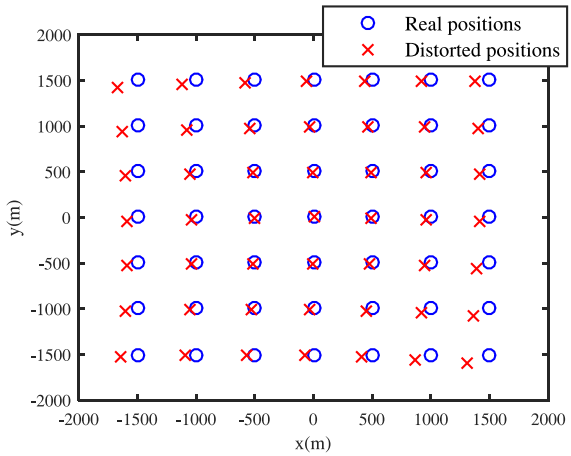

Fig. 3. Real targets area and the corresponding distorted positions in a final image of PFA. Blue dots represent real target positions while red crosses represent the distorted positions.

Note that in this section, we are only concerned about the changing of the curvature phase φ_p with the space variables (x, y), so the variables (f_τ, t) are omitted here in the expression of $\varphi_p(f_\tau, t; x, y)$.

First, when applying PFA on a point target $P(x_p, y_p)$ without any additional processing, its impulse response will occur at a distorted position $(\hat{x}, \hat{y})$. As presented in Section III, the signal phase of point target P before the polar format mapping is $\varphi_p(x_p, y_p)$ given by (10). That means for PFA, a signal phase $\varphi_p(x_p, y_p)$ corresponds to an impulse response position $(\hat{x}, \hat{y})$ in the final image. This can be expressed as

$$\varphi_p(x_p, y_p) \Rightarrow (\hat{x}, \hat{y}). \tag{16}$$

Second, if we compensate $\varphi_p(x_p, y_p)$ for the conjugate curvature phase of (x_p, y_p), the signal phase will become actually $\hat{\varphi}(f_\tau, t)$ without the curvature phase error $\varphi_{\text{cur}}(f_\tau, t)$ [these two expressions are mentioned in (10)], and what's more, the position error will be removed and the impulse response will occur at the correct position (x_p, y_p). Here, we regard $\hat{\varphi}(f_\tau, t)$ as $\hat{\varphi}(x_p, y_p)$, since its corresponding target position is(x_p, y_p), thus we know a signal phase $\hat{\varphi}(x_p, y_p)$ corresponds to an impulse response position (x_p, y_p). Furthermore, if the signal phase before the polar format mapping of a certain point target is $\hat{\varphi}(\hat{x}, \hat{y})$, its corresponding impulse response position in the final PFA image is $(\hat{x}, \hat{y})$. This can be expressed as

$$\begin{gathered} \hat{\varphi}(x_p, y_p) \Rightarrow (x_p, y_p) \\ \Downarrow \\ \hat{\varphi}(\hat{x}, \hat{y}) \Rightarrow (\hat{x}, \hat{y}). \end{gathered} \tag{17}$$

As we know, only the zeroth- and first-order terms of $\varphi(t; x, y)$ have influence on the impulse response position, thus we can infer from (16) and (17) that

$$\begin{aligned} \hat{\varphi}_0(\hat{x}, \hat{y}) &= \varphi_{p0}(x_p, y_p) \\ \hat{\varphi}_1(\hat{x}, \hat{y}) &= \varphi_{p1}(x_p, y_p) \end{aligned} \tag{18}$$

where

$$\hat{\varphi}_0(\hat{x}, \hat{y}) = -2\pi \frac{f_c + f_\tau}{c} \Delta \hat{R}_p(0; \hat{x}, \hat{y}) \tag{19a}$$

$$\hat{\varphi}_1(\hat{x}, \hat{y}) = -2\pi \frac{f_c + f_\tau}{c} \frac{\partial \Delta \hat{R}_p(t; \hat{x}, \hat{y})}{\partial t}\bigg|_{t=0} \tag{19b}$$

$$\varphi_{p0}(x_p, y_p) = -2\pi \frac{f_c + f_\tau}{c} \Delta R_p(0; x_p, y_p) \tag{19c}$$

$$\varphi_{p1}(x_p, y_p) = -2\pi \frac{f_c + f_\tau}{c} \frac{\partial \Delta R_p(t; x_p, y_p)}{\partial t}\bigg|_{t=0} \tag{19d}$$

All the results in (19) are constant with respect to t and (19a), (19b) are both linear with respect to $(\hat{x}, \hat{y})$ while (19c), (19d) are both complicated functions with respect to (x_p, y_p). Thus, (18) can be simplified as

$$\begin{aligned} B_{x0}\hat{x} + B_{y0}\hat{y} &= C_0(x_p, y_p) \\ B_{x1}\hat{x} + B_{y1}\hat{y} &= C_1(x_p, y_p) \end{aligned} \tag{20}$$

where the expressions of these six coefficient terms are all given in the Appendix.

It can be clearly seen that (20) is a binary linear equation group with respect to $(\hat{x}, \hat{y})$. Its solution is given by

$$\begin{aligned} \hat{x} &= \left[C_1(x_p, y_p)D_x - C_0(x_p, y_p)\right]/E_x \\ \hat{y} &= \left[C_1(x_p, y_p)D_y - C_0(x_p, y_p)\right]/E_y \end{aligned} \tag{21}$$

where

$$D_x = B_{y0}/B_{y1} \tag{22a}$$

$$D_y = B_{x0}/B_{x1} \tag{22b}$$

$$E_x = B_{x1}B_{y0}/B_{y1} - B_{x0} \tag{22c}$$

$$E_y = B_{y1}B_{x0}/B_{x1} - B_{y0}. \tag{22d}$$

Thus, we obtain the relationship between distorted coordinates and their corresponding real coordinates for PFA. Fig. 3 shows the distorted point positions of a rectangular targets array. This result can be used for geometric distortion correction through 2-D interpolation. But as will be seen in the next section, the proposed curvature error correction method can solve the defocusing effect and geometric distortion simultaneously, so interpolation correction is not needed. In addition, this result plays another important role in the proposed wavefront curvature correction.

B. Defocusing Effect and Scene Size Limits for BiSAR PFA

As the major problem for PFA in BiSAR imaging processing, the curvature phase error will induce defocusing effect, which becomes more severe as the scene size becomes larger. If wavefront curvature correction is not applied, we need to limit the imaging scene size to guarantee the effectiveness of imaging.

As mentioned in Section A, the second-order component of the curvature phase plays a major role in defocusing for PFA. Therefore, the scene size limits can be derived based on the second-order phase error also called QPE.

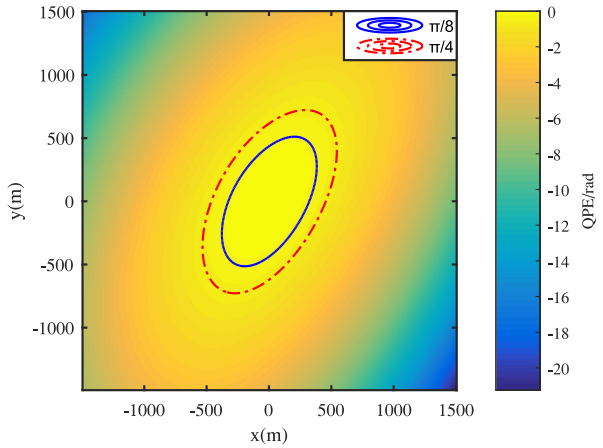

Fig. 4. Distribution of QPE for a high-speed maneuvering platform Bistatic forward-looking configuration. The blue full line is the boundary inside which the QPE is less than $\pi/8$ while the red dashdotted line is the boundary inside which the QPE is less than $\pi/4$.

Since the variance of range frequency $(f_c + f_\tau)$ can be ignored compared to the carrier frequency, we can approximately set f_τ to zero and thus the QPE can be written as a binary function with respect to (x_p, y_p)

$$\begin{aligned}&\varphi_q(x_p, y_p)\\ &= -\frac{2\pi}{\lambda}\left(\frac{T_a}{2}\right)^2 \frac{\partial^2 \Delta R_p(t; x_p, y_p)}{2\partial t^2}\bigg|_{t=0}\\ &= -\frac{\pi {T_a}^2}{4\lambda}\left(\sum_{i=0}^{2} Q_i x_p^{2-i} y_p^i + \sum_{i=0}^{3} T_i x_p^{3-i} y_p^i\right)\end{aligned} \tag{23}$$

where the coefficients Q_i and T_i are presented in the Appendix.

Obviously, the QPE gets larger as the target gets further from the scene center. In order to compute the limits on x_p and y_p for focusing effect, a threshold φ_{TH} for QPE is needed, which is often considered as $\pi/4$. That means when $|\varphi_q(x_p, y_p)|$ is larger than φ_{TH}, the image is judged as unfocused. Then, the scene size limits can be written as

$$\left|\sum_{i=0}^{2} Q_i x_p^{2-i} y_p^i + \sum_{i=0}^{3} T_i x_p^{3-i} y_p^i\right| < \frac{4\lambda\varphi_{\text{TH}}}{\pi {T_a}^2}. \tag{24}$$

The exact limits for x_p and y_p can be obtained by numerically solving this binary inequation for a group of given parameters. Fig. 4 shows the distribution diagram of QPE for a certain forward-looking case (the relevant parameters are given in Section VI). When a threshold for QPE is given, an area with an approximated ellipse shape can be marked out inside, which the QPE is small enough and thus the focusing effect is acceptable. If the needed scene size exceeds the limits, wavefront curvature correction is needed.

In addition, the actual size of the imaging scene is recommended to be smaller than the $\pi/4$ limits to keep the image well focused. Therefore, we choose $\pi/8$ as the scene size limits in the following works.

In the proposed wavefront curvature correction, the phase compensation filter is space-variant, but we do not need to update the parameters of the filter at every position. Instead, we can adopt the same parameters for the compensation within an area whose size can as well be determined by solving (24). This will be discussed in detail in the next section.

V. Space-Variant Phase Compensation for Wavefront Curvature in Wavenumber-Domain

As discussed in the previous section, when the imaging scene size is large enough so that the QPE cannot be neglected, curvature error correction is necessary.

It is obvious that compensating for the curvature phase error with one certain position (x_p, y_p) cannot broaden the effective imaging scene size, since the phase error is space-variant. To effectively correct the wavefront curvature error, the phase compensation should be carried out after obtained the PFA image that is in space-domain, as we can conveniently differentiate targets at different positions. Since the spatial frequency domain is equated with wavenumber domain, the compensation filter should be designed in wavenumber domain, which can be obtained by transforming the curvature phase according to the polar format mapping (11). But before that, in order to avoid vast numerical computation, we need to analytically derive the expression of the curvature phase in wavenumber domain.

A. Wavenumber-Domain Phase Compensation Filter

As mentioned in Section III, the curvature phase error in wavenumber-domain is written as $\varphi_{\text{cur}}(k_x, k_y)$ in (13), which is the result of the polar format mapping given by (11) from $\varphi_{\text{cur}}(f_\tau, t)$. In order to obtain the analytical expression of $\varphi_{\text{cur}}(k_x, k_y)$, we need to derive the inverse function of (11). However, the polar format mapping is a complicated binary function, whose inverse function is usually hard to obtain. But note that the two equations in (11) have a common factor k_r, so we can first derive the inverse function with respect to t by using series reversion [30].

Divide k_y by k_x and perform a Taylor expansion up to third order with respect to t on this fraction, then we have

$$\begin{aligned}\frac{k_y}{k_x} &= \frac{y_T(t)R_R(t) + y_R(t)R_T(t)}{x_T(t)R_R(t) + x_R(t)R_T(t)}\\ &\approx A_0 + A_1 t + A_2 t^2 + A_3 t^3.\end{aligned} \tag{25}$$

The expression of k_y/k_x in azimuth time domain is too complicated to derive its Taylor expansions analytically. Instead, we calculate these coefficients directly through numerical approach. Let $k_y/k_x = f(t)$, then these coefficients can be expressed as

$$A_0 = f(0) \tag{26a}$$

$$A_1 = f^{'}(0) \tag{26b}$$

$$A_2 = \frac{1}{2} f^{''}(0) \tag{26c}$$

$$A_3 = \frac{1}{6} f^{'''}(0). \tag{26d}$$

Then, use series reversion on the series in (25), we have

$$t(k_x,k_y)\approx\frac{1}{A_1}\left(\frac{k_y}{k_x}-A_0\right)-\frac{A_2}{A_1^3}\left(\frac{k_y}{k_x}-A_0\right)^2+A_1^{-5}(2A_2^2-A_1A_3)\left(\frac{k_y}{k_x}-A_0\right)^3. \quad (27)$$

Substitute (27) into k_x given in (11a), we have

$$k_r(k_x,k_y)=\frac{k_xR_T(t)R_R(t)}{x_T(t)R_R(t)+x_R(t)R_T(t)}\approx\frac{k_xR_T\left[t(k_x,k_y)\right]R_R\left[t(k_x,k_y)\right]}{\left\{\begin{array}{l}x_T\left[t(k_x,k_y)\right]R_R\left[t(k_x,k_y)\right]\\+x_R\left[t(k_x,k_y)\right]R_T\left[t(k_x,k_y)\right]\end{array}\right\}}. \quad (28)$$

Thus, we obtain the expression of the inverse function of k_x and k_y with respect to t and k_r. Substitute (27) and (28) into $\varphi_{\text{cur}}(f_\tau,t)$, then we can obtain the expression of the curvature phase in 2-D wavenumber domain and thus can compensate for it in this domain. The space-variant wavenumber domain filter can be expressed as

$$H_{\text{svc}}(k_x,k_y;x_p,y_p)=\exp\left\{jk_r(k_x,k_y)\Delta\hat{R}_{\text{cur}}\left[t(k_x,k_y);x_p,y_p\right]\right\}. \quad (29)$$

For space-variant correction, the uncompensated PFA image needs to be divided into several subblocks and then we can multiply the spectra of them by the compensation filter with the parameters updated at their center positions, respectively. After that, the final image can be obtained by splicing these compensated subblocks.

To make the compensation effective, the size of each subblock must be small enough to keep the space-variance of the curvature phase inside each subblock weak enough. However in some applications, the distortion of the PFA image may be severe. In such conditions, a certain target actually located in one subblock will probably occur in an adjacent subblock. This will lead to a garble output image, unless we set a high overlap rate for these subblocks. To solve this problem, an efficient realization of space-variant filtering based on two-stage division is designed and presented in the next section.

B. Space-Variant Filtering Using Two-Stage Image Division

In this section, we first present the procedures of the two-stage division realization. It will be seen at the end of this section how this realization can reduce the overlap rate and thus improve the efficiency of wavefront curvature correction.

1) Divide the whole PFA image into several subblocks which are of the same size and have no intersection. These subblocks are called the original blocks and each original block has a corresponding subimage that contains and is larger than the original block. To solve the distortion problem, we let every two adjacent subimages overlapped and the overlap rate should be high enough to keep them larger than the distorted output of their corresponding original area. This step can be expressed as

$$\begin{aligned}h(x,y)&=\bigcup_{m=1}^{M}h_m(x,'y')\\&=\bigcup_{m=1}^{M}\hat{h}_m(\hat{x},'\hat{y}')\end{aligned} \quad (30)$$

where $h(x,y)$ is the whole image of PFA, h_m represents each original block, $\hat{h}_m$ is the corresponding subimage, and M is the number of subimages. The size of each subimage corresponds to the value range of $(\hat{x},'\hat{y}')$, which can be determined by using the expression of distorted coordinates with respect to real coordinates given in (21). Suppose a subimage corresponds to a real position range of $[x_0-x_I,x_0+x_I]$ and $[y_0-y_I,y_0+y_I]$, the coordinate ranges of this subimage can be computed by substitute the real positions of the four corners into (21) and find the largest distortion in both x and y directions. The subimages may have different sizes as long as they satisfy their own limits.

2) Partition each original block into several subregions, while no need to divide the corresponding subimage data. This can be written as

$$h_m(x,'y')=\bigcup_{n=1}^{N}h_{m,n}(x,''y'') \quad (31)$$

where $h_{m,n}$ represents the nth subregion of the mth original block and N is the number of subregions in each block. The size of the subregions should be small enough to keep the space-variance within each region weak enough. In fact, these size limits are consistent with the scene size limits of PFA derived in Section IV, because compensating for the curvature phase with respect to the center of a certain region is equivalent to performing uncorrected PFA using this center position as reference, in terms of focusing effect. Thus, the size limits of each subregion can be obtained by solving the inequation (24). This is hard to realize, but usually there is a certain proportion between the sizes of the two dimension of a processed image, as well as the subimages and the subregions. Suppose the sizes of a subregion are $d_x\times d_y$ and $d_x=kd_y$, using (24) we have

$$\left|\sum_{i=0}^{2}Q_ik^{2-i}d_y^2+\sum_{i=0}^{3}T_ik^{3-i}d_y^3\right|<\frac{4\lambda\varphi_{\text{TH}}}{\pi{T_s}^2}. \quad (32)$$

This inequation can be solved by using the radical formula of simple cubic equation, thus the limits of d_x,d_y can be obtained. However, note that due to the space-variance of echo signal, the effective focusing sizes at different positions are also variant. For processing convenience, it is recommended to set a unified size for each subregion, so we need to find the smallest size limits determined by (32). Fig. 5 shows the $\pi/4$ QPE limits at positions of the scene center and the four corners of the whole scene (the relevant parameters are identified as those are used in the simulations). As can be seen, the black ellipse that denotes the size limits at the scene center turns out to be

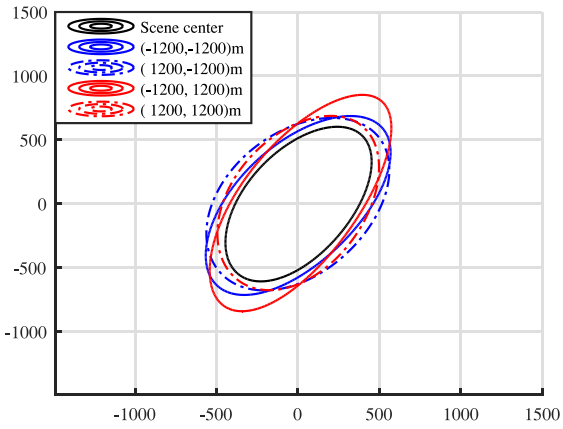

Fig. 5. Size limits of the subregions at five different positions. All the ellipses are figured together at the center for comparison.

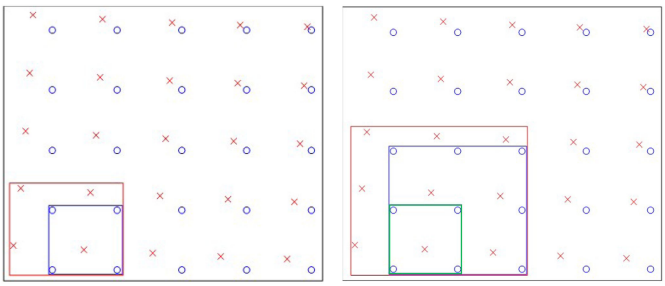

Fig. 6. Comparison between traditional image division and the proposed two-stage division. (a) Traditional image division. (b) Two-stage image division.

the smallest, thus we can set the same limits for the other subregions to carry out the correction.

3) For each subregion in an original block, update the parameters of the compensation filter and perform the curvature error correction. This procedure is a combination of curvature phase compensation and residual geometric distortion correction. The phase compensation, obviously, is done in wavenumber-domain by multiplication. Here, we give a simple description of the combined distortion correction steps.

The geometric distortion of any subregion can be regarded as the sum of a bulk shift (equal to the region center) and a residual distortion. The bulk shift can be simultaneously removed in the curvature phase compensation. For the residual distortion, as each subregion is relatively small, the complicated distortion, whose expression is given by (21), can be approximated as a binary quadratic equation group,

$$\hat{x} - x_p = a_x \Delta y + b_x \Delta y^2 \tag{33a}$$

$$\hat{y} - y_p = a_y \Delta x + b_y \Delta x^2 \tag{33b}$$

where (x_p, y_p) is the center position of a subregion and a_x, a_y, b_x, and b_y can be simply obtained through polynomial

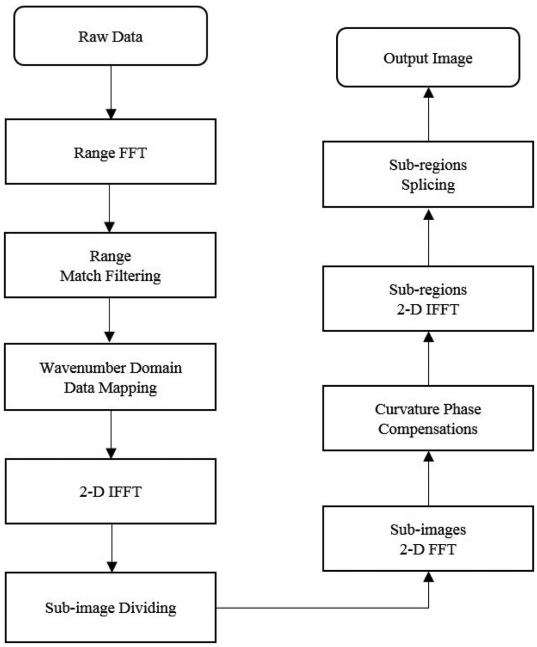

Fig. 7. Flowchart of the proposed algorithm, including PFA and the proposed wavefront curvature compensation.

fitting on the formulas (21). The error is verified to be within one image pixel.

Using the simplified distortion formulas, the residual distortion correction can be realized by data shifting along the two dimensions, respectively. This shifting can be easily done through linear phase term multiplication in frequency-domain, and the two phase terms are given by

$$\varphi_{gx}(k_x, y) = \exp\left\{jk_x\left[a_x(y - y_p) + b_x(y - y_p)^2\right]\right\} \tag{34}$$

$$\varphi_{gy}(x, k_y) = \exp\left\{jk_y\left[a_y(x - x_p) + b_y(x - x_p)^2\right]\right\}. \tag{35}$$

Now, we present the complete steps of this procedure. First, multiply the 2-D FFT of the corresponding subimage of that block by the filter to each subregion,

$$H'_{m,n} = H_m(k_x, k_y) \times H'_{svc}(k_x, k_y; x_{m,n}, y_{m,n}) \tag{36}$$

where $H'_{m,n}$ represents the wavenumber spectrum of the filtered nth subregion in the mth original block, H_m is the 2-D FFT of the mth subimage and $(x_{m,n}, y_{m,n})$ is the center position of this subregion. H'_{svc} is the downsampled version of H_{svc} whose size is consistent with its corresponding subimage data and a linear phase factor is adding to it to compensate for the offset of the image center After that, transform the filtered wavenumber spectra into $k_x - y$ domain, where the IFFT computation is over the corresponding subregion only. Next, compensate the phase term φ_{gx}. Then, transform it into $k_y - y$ domain, compensate the phase term φ_{gx} and last transform into 2-D space domain over the specified subregion only. This

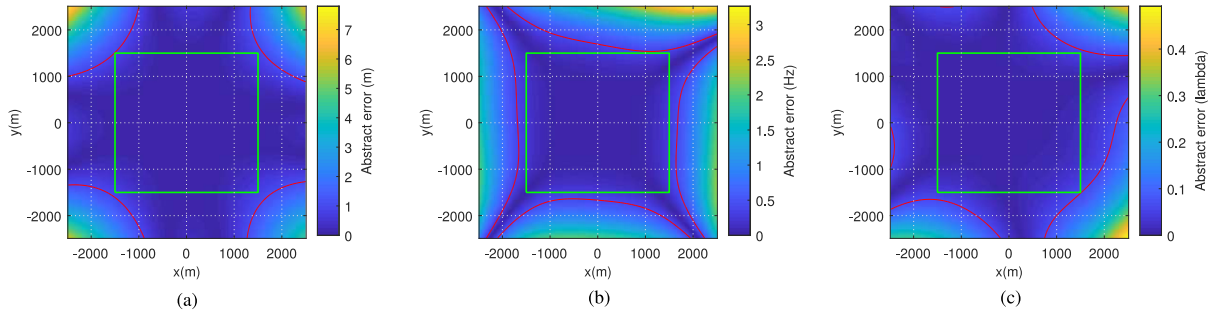

Fig. 8. Spatial distribution of the residual error of the presented curvature range error model. Red lines are the boundaries of the thresholds. Same green rectangles that represent a 3000 × 3000 m area are marked out in all the figures. (a) Zeroth-order error. (b) Ratio of first-order error to λ. (c) Product of second-order error and $T_a^2/4$.

series of steps can be expressed as

$$H_x = \exp\left(j\varphi_{gx}(k_x, y)\right) \cdot F_y^{-1}\left\{H'_{m,n}\right\}\Big|_{y\in Y_{m,n}} \quad (37a)$$

$$H_y = \exp\left(j\varphi_{gx}(x, k_y)\right) \cdot F_x^{-1}\left\{F_y\left\{H_x\right\}\right\}\Big|_{x\in X_{m,n}} \quad (37b)$$

$$h'_{m,n}(x, y) = F_y^{-1}\left\{H_y\right\} \quad (37c)$$

where $F_y\{\cdot\}$ and $F_y^{-1}\{\cdot\}$ denote FFT and inverse FFT, $X_{m,n}, Y_{m,n}$ represents the value range of x, y in the nth subregion of the mth original block and $h'_{m,n}$ is the curvature error correction result of this subregion.

Note that in this procedure, when computing the filtering output for each subregion, the size of the multiplier input is several times larger than the IFFT output. This will result in extra computational burden. In fact, according to the properties of discrete time fourier transform (DTFT), we can ulteriorly down-sample H'_{svc} together with H_m to the same size as $h'_{m,n}$, which leads to a periodical extension in space-domain. This periodical extension has no influence on the series of results from (37), since we only compute a single period (refers to $X_{m,n}, Y_{m,n}$) of the inverse DTFT. In addition, a linear phase factor must be added to the ulteriorly down-sampled H'_{svc} to compensate for the image center offset between the subregion and the subimage.

4) Repeat the above procedures for all the subimages, then the whole output image can be obtained by combining all the compensated output of the subregions, which can be expressed as

$$h'(x, y) = \bigcup_{m=1}^{M}\left(\bigcup_{n=1}^{N} h'_{m,n}\right) \quad (38)$$

where $h'(x, y)$ denotes the whole compensated image that is well focused and geometric undistorted.

The difference between the proposed realization and traditional image division realization can be indicated in Fig. 6. In Fig. 6(a), the blue rectangle denotes an original image area and the red one denotes the corresponding distorted image area. In Fig. 6(b), the red rectangle denotes a subimage, the blue one denotes the corresponding original block and the green one denotes a subregion in this block. It can be seen that for the traditional division method, the ratio of the distorted area to the original area is relatively high, while for the proposed division method, the ratio of the subimage to the original block is relatively low. Thus, the needed overlap rate for the proposed realization can be reduced compared to traditional image division method, while no extra computational burden is induced. As a quantitative example under our simulation parameters given in Section VI, the total overlap rate the traditional realization for the nine points in the left bottom is 35%. By comparison, the overlap rate in the proposed realization is only 22%. If the geometric distortion is more severe, this difference will get even larger.

Fig. 7 shows the flowchart of the proposed algorithm.

TABLE I
SIMULATION PARAMETERS

Geometry Parameters	Transmitter	Receiver
Center Location $\vec{L}_0=(x_0,y_0,z_0)$	(10,0,0.8) km	(0,-10,0.8) km
Velocity $\vec{v}=(v_x,v_y,v_z)$	(80,20,0)m/s	(0,80,0)m/s
Acceleration $\vec{a}=(a_x,a_y,a_z)$	(-6,8,0)m/s^2	(0,6,-6)m/s^2
Jerk $\vec{j}=(j_x,j_y,j_z)$	(2,0,0)m/s^3	(0,0,2)m/s^3
Trajectory $\vec{r}(t)=[x(t),y(t),z(t)]$	$\vec{L}_0+\vec{v}t+\frac{1}{2}\vec{a}t^2+\frac{1}{3}\vec{j}t^3$	

System Parameters	
Carrier Frequency f_c	9.6GHz
Signal Bandwidth B_r	100MHz
PRF f_p	1000Hz
Synthetic Aperture Time T_s	2.5s

C. Limitations

The main limitations of our proposed imaging method come from the third-order approximation of the curvature range error given by (14) and (15). To illuminate the application sphere of this approximation, we present analysis on it.

Fig. 8 shows the spatial distribution of the residual error of the three orders of components (with respect to azimuth time) from the curvature range error model. Since we expect the residual error to have little influence on the subsequent processing, the

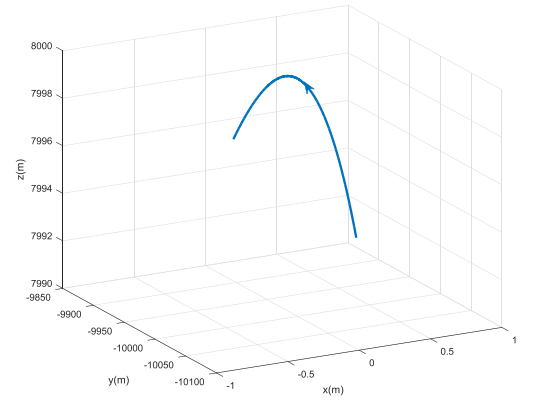

(a)

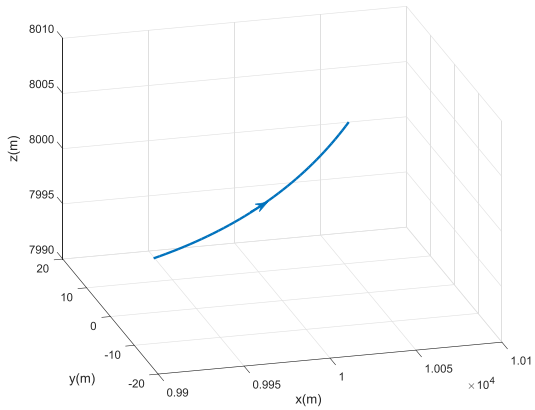

(b)

Fig. 9. Trajectories of the radar platforms. (a) Receiver. (b) Transmitter.

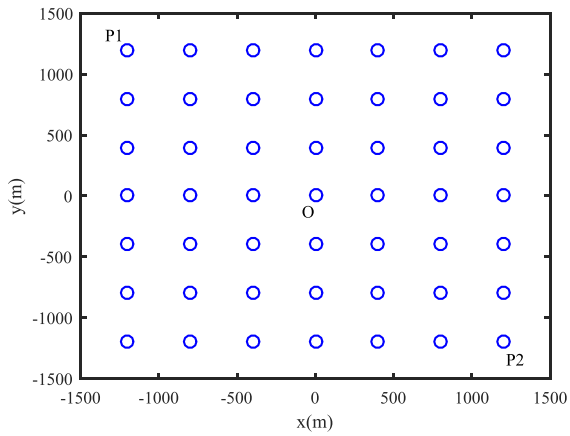

Fig. 10. Target area used in the simulations.

thresholds of the zeroth, first and second-order components are set as follows.

1) Zeroth-order error. This component represents the error of range measurement, so the threshold is set as 1 m. Shown in Fig. 8(a).

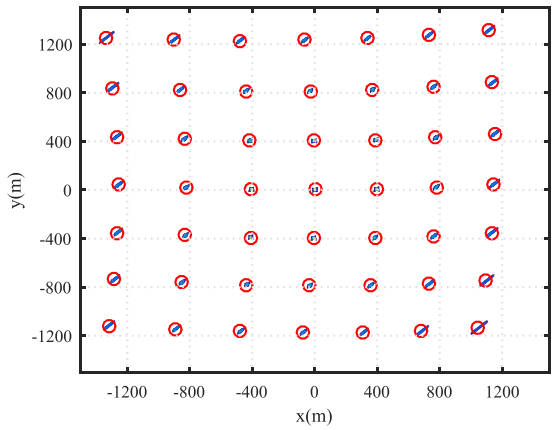

Fig. 11. Comparison between the distorted positions computed through the result given in (21) and the simulated imaging result for the 49 point targets. The red circles denote the computed distorted positions and the real positions are at the intersection points of the grids.

2) First-order error. The ratio of this component to the wavelength λ represents the error of Doppler centroid measurement, so the threshold of this ratio is set as 0.4 Hz. Shown in Fig. 8(b).
3) Sencod-order error. The product of this component and the square of a half synthetic aperture time T_a affects the focusing effect, whose threshold is set as $\lambda/16$. Shown in Fig. 8(c).

As can be seen, under our simulation parameters with about only 10 km operating range, the error of curvature range model is small enough in over 3000 $\times$ 3000 m area.

VI. Simulations

In this section, we present the point target simulations to verify the proposed results in Sections IV and V. Simulations are carried out in a forward-looking case that both the transmitter and the receiver fly with curved trajectories that are third order with respect to azimuth time. The relevant simulation parameters are given in Table I and the sketches of the platform trajectories are shown in Fig. 9.

The imaging scene is set as a 7 $\times$ 7 point array as shown in Fig. 10. The distances between every two adjacent point targets along both x-and y-directions are 400 m while the size of the whole area is 2.4 $\times$ 2.4 km. P_1 and P_2 are two targets located at the corners of the scene where the curvature errors are the largest (according to the distribution of QPE). O is at the center of the area and is set to be the reference point.

A. Simulation for the Geometric Distortion Analysis

Fig. 11 gives the image result for the whole target area using original BiSAR PFA. The distorted positions computed through the result given in (21) of the 49 targets are marked out. It can be seen that the positions of all the impulse responses are consistent with the computed distorted positions.

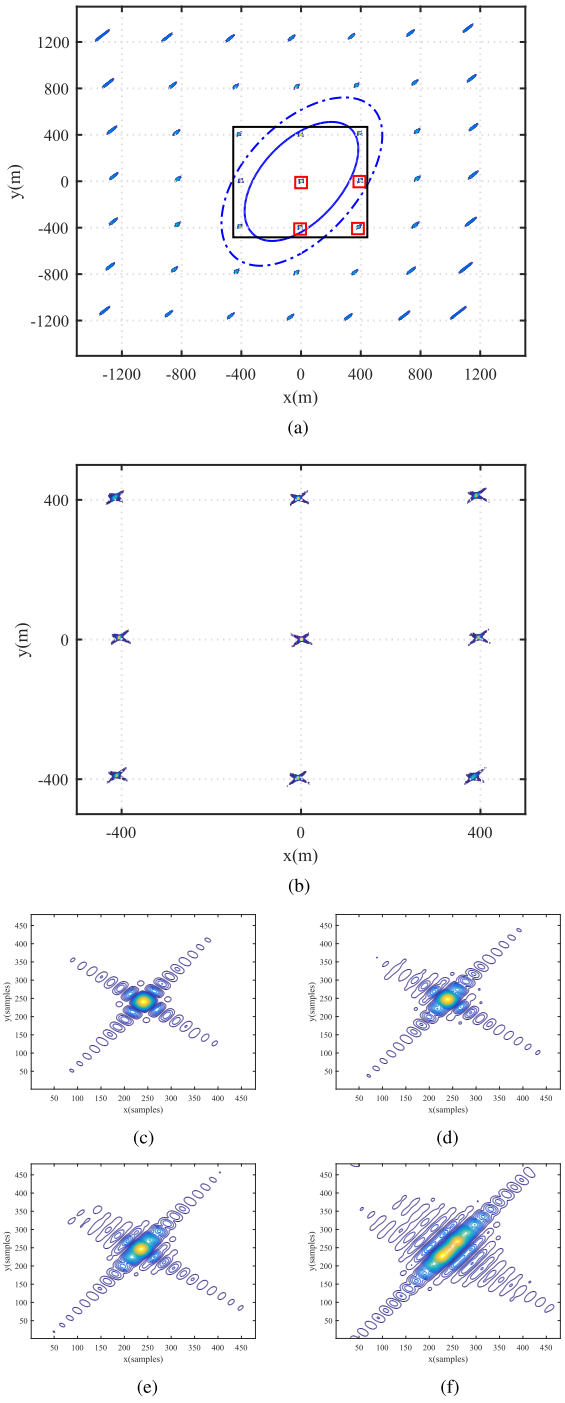

Fig. 12. Scene size limits simulations. (a) is the whole uncompensated PFA image and the regions where QPE is less than $\pi/4$ and $\pi/8$ are marked out by blue lines while the selected enlarged region is marked out by black rectangle. (b) is the partial enlarged image for the selected region. (c)–(f) are the azimuth profiles of the four selected targets. (a) Full view. (b) Selected region. (c) Target O. (d) Target at $(0, -400)$ m. (e) Target at $(-400, 0)$ m. (f) Target at $(-400, 400)$ m.

B. Simulations for the Derived Scene Size Limits

Fig. 12 shows the scene size limits given by (24). The regions where QPE is less than $\pi/4$ and $\pi/8$ are marked out by the blue lines and a rectangular region is selected to indicate the defocusing effect. Among the targets in the selected region, we select four targets which are at the scene center, inside but near

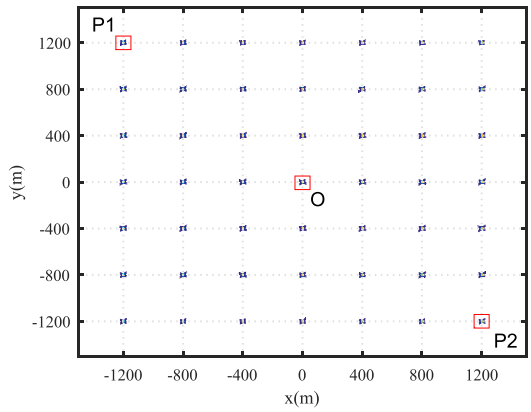

Fig. 13. Full view of the whole imaging result after applying the proposed wavefront curvature compensation. Four selected are marked out by blue rectangles. Three selected point targets P_1, P_2, and O are marked out by red rectangles.

the boundary of the $\pi/8$ region, outside the $\pi/8$ region but inside the $\pi/4$ region and outside the $\pi/4$ region, respectively, and present their contours. It can be seen that the focusing effect for the four targets in azimuth direction gets worse and worse. The focusing effect is just tolerable for the two targets near the boundary of the $\pi/8$ region while poor for the target outside the $\pi/4$ region. What's more, the position error of these targets except the center one all exceeds 5 m, which can be seen in Fig. 12(b) and is unacceptable. Therefore, we decide to take 400×400 m which is right within the $\pi/8$ region as the scene size limit.

C. Point Target Simulations for the Proposed Imaging Method

To verify the effectiveness of the proposed method, we give both the full view of the imaging result and analysis for three representative point targets in more detail. A brief comparison of the impulse responses with the wavefront curvature correction method in [27] and a recent proposed imaging method [31] is carried out as well. For convenience, we use "Wang's method" to denote the method proposed in [27] and "Deng's method" to denote the one in [31] in the following part.

In this simulation for the proposed method, the size of each subregion is set to be 400×400 m while the number of subimages is 9 and the sizes of all the subimages are set to be 1000×1000 m to cover all the needed targets. Each subimage contains four subregions.

Fig. 13 gives the full view of the imaging result. P_1, P_2, and O are the three representative point targets, which locate at the bottom left corner, the top-right corner and the center of the whole target area. O is set to be the reference point and the space-variances of Doppler phase of P_1 and P_2 relative to the reference point are the most severe among all the targets. Fig. 14 gives the comparison of the impulse responses contours among the proposed method, Wang's method and Deng's method for the three representative point targets, while Fig. 15 gives the comparison of the azimuth profiles between the proposed method and Deng's method (because Deng's method is better than Wang's method in terms of focusing effect). It can be seen

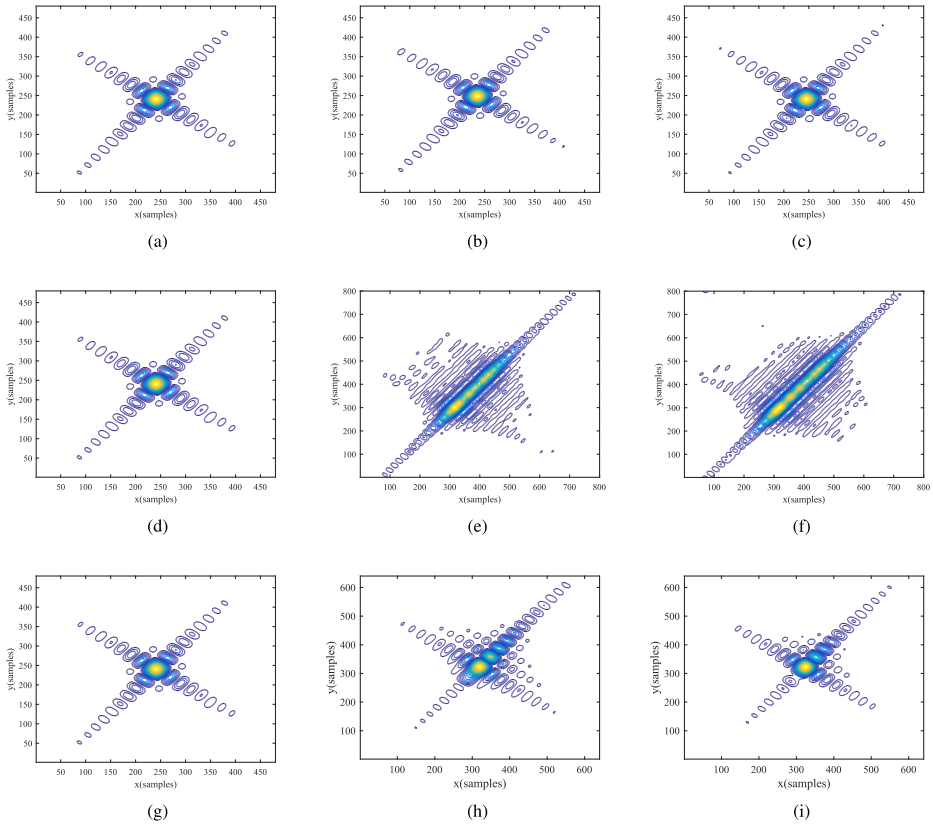

Fig. 14. Comparison of contours among the proposed method, Wang's method and Deng's method for Target O, P_1 and P_2. (a)–(c) the proposed method. (dw)–(f) Wang's method. (g)–(i) Deng's method. (a) Target O. (b) Target P_1. (c) Target P_2. (d) Target O. (e) Target P_1. (f) Target P_2. (g) Target O. (h) Target P_1. (i) Target P_2.

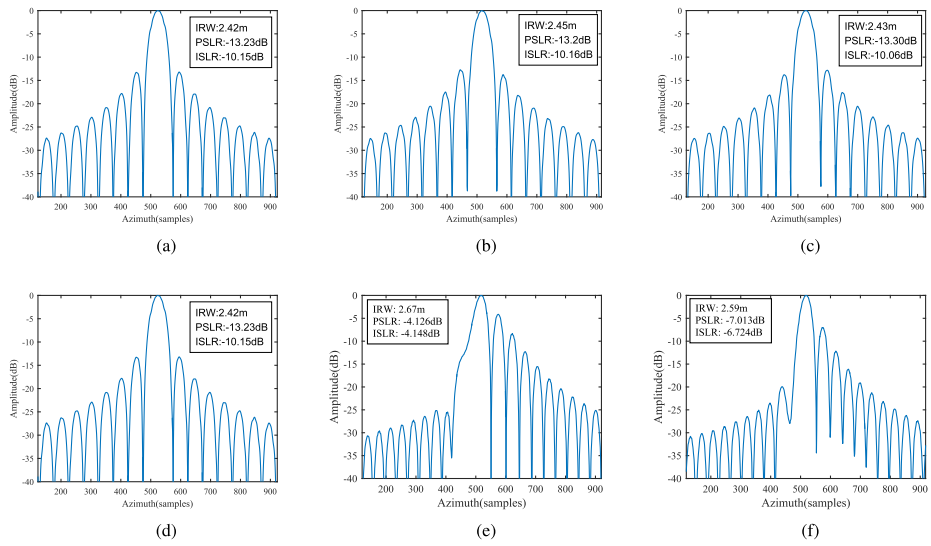

Fig. 15. Comparison of profiles in azimuth direction between the proposed method and Deng's method for O, P_1 and P_2. (a)–(c) the proposed method. (d)–(f) Deng's method. (a) Target O. (b) Target P_1. (c) Target P_2. (d) Target O. (e) Target P_1. (f) Target P_2.

that the focusing effect for P_1 and P_2 of the proposed method is almost as good as that of the reference point O. Wang's method can only slightly improve the focusing effect and the results remains unfocused, since it is derived for linear flight paths. Deng's method can obtain good focusing effect on the main lobes but the side lobes can be seen seriously asymmetric. Moreover, Deng's method adopt a point-by-point structure to handle the space-variation, which results in large computational burden.

These results indicates that the proposed method can work pretty well for general BiSAR even with third-order platform trajectories.

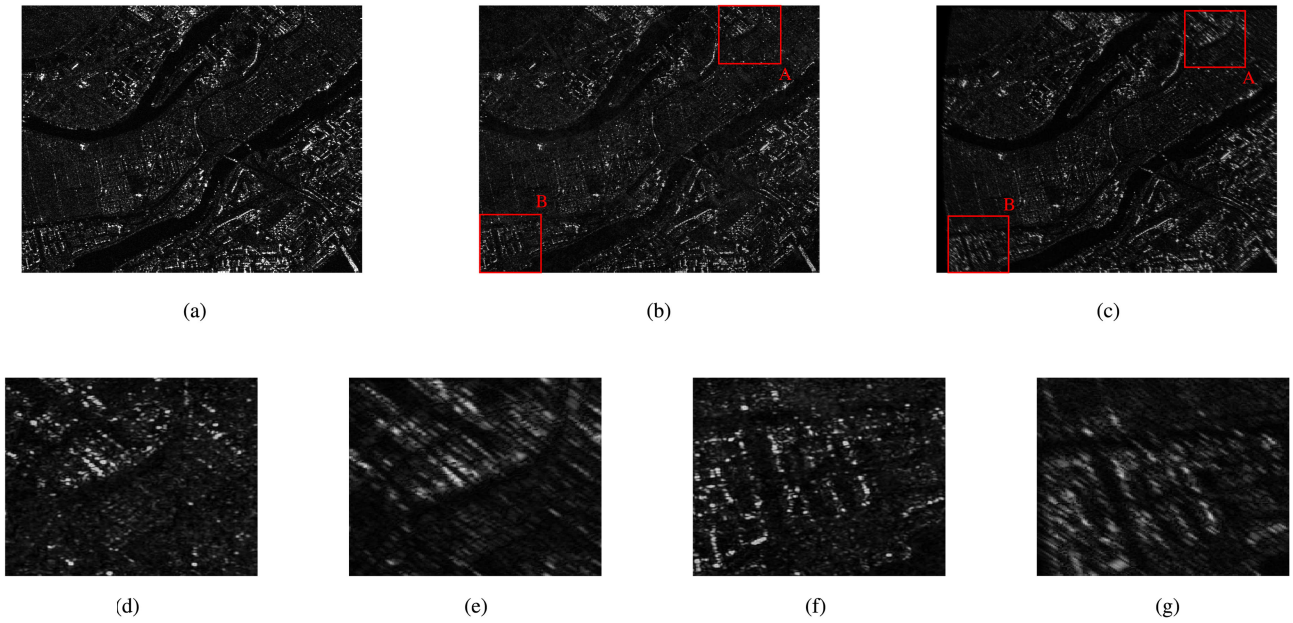

Fig. 16. Comparison of the imaging results between the proposed method and Wang's method. (a) Original target scene. (b) Imaging result of the proposed method. (c) Imaging result of Wang's method. (d) Area A of the proposed method. (e) Area A of Wang's method. (f) Area B of the proposed method. (g) Area B of Wang's method.

D. Extended Target Simulations for the Proposed Imaging Method

In order to further verify the effectiveness of the proposed imaging method, we present the extended target simulation result and give the comparison with Wang's method. Partial enlarged images of the two corners in the original image are given to indicate the difference in focusing effect. In addition, these simulations are carried out under the same parameters as the point targets simulations in the previous sections and the size of the simulated scene is as well 2400 $\times$ 2400 m.

As can be seen in Fig. 16, the result processed by the proposed method is almost identical to the original image, while the one processed by Wang's method suffers significant degrading in the edges of the scene and what's more there exists obvious geometric distortion. These simulation results well indicates that the proposed method can greatly expand the effective scene size for BiSAR with complicated flight paths compared with the existing results of PFA and meanwhile eliminate geometric distortion.

VII. Conclusion

A generalized wavefront-curvature-corrected PFA for BiSAR with complicated flight paths is presented in this article. The original PFA for BiSAR is reviewed and analyzed. The geometric distortion mapping and the scene size limits for the original PFA are derived analytically. The proposed wavefront curvature correction is based on the analytical expression of the curvature phase error derived through method of series reversion, and an efficient realization of the space-variant correction is proposed based on the conclusions from the analysis of BiSAR PFA. A phase compensation for the geometric distortion are combined with the space-variant correction procedures, thus no extra interpolation for the distortion correction is needed in our method. All the presented results are theoretically applicable for general BiSAR with arbitrary finite order trajectories, and simulation results show that the proposed results are effective for BiSAR with up to third-order trajectories. Furthermore, even when the platforms are with irregular motion, the proposed method can also work well through polynomial fitting as long as the trajectories can be approximated as finite-order polynomials of azimuth time.

Appendix A
Coefficients Used in Curvature Error Analysis

In this appendix, we give the coefficients used in curvature error analysis in Section IV. These coefficients include $B_{x0}, B_{x1}, B_{y0}, B_{y1}, C_0, C_1$ and $Q_0, Q_1, Q_2, T_0, T_1, T_2, T_3$.

The coefficients used in the expression of the distorted coordinates are given in (39).

$$B_{x0} = -\frac{x_R(0)}{R_R(0)} - \frac{x_T(0)}{R_T(0)} \tag{39a}$$

$$B_{y0} = -\frac{y_R(0)}{R_R(0)} - \frac{y_R(0)}{R_R(0)} \tag{39b}$$

$$B_{x1} = -\left.\frac{d\left[x_R(t)/R_R(t)\right]}{dt}\right|_{t=0} - \left.\frac{d\left[x_T(t)/R_T(t)\right]}{dt}\right|_{t=0} \tag{39c}$$

$$B_{y1} = -\left.\frac{d\left[y_R(t)/R_R(t)\right]}{dt}\right|_{t=0} - \left.\frac{d\left[y_T(t)/R_T(t)\right]}{dt}\right|_{t=0} \tag{39d}$$

$$C_0 = R_{Tp}(0) - R_{T0}(0) - R_{Rp}(0) - R_{R0}(0) \tag{39e}$$

$$C_1 = \left.\frac{d\left[R_{Tp}(t) - R_{T0}(t) + R_{Rp}(t) - R_{R0}(t)\right]}{dt}\right|_{t=0}. \tag{39f}$$

The coefficients used in the scene size limits are given as follows:

$$Q_0 = \partial^2 \left.\frac{\left[y_R(t)^2 + z_R(t)^2\right]}{4R_R(t)^3}/\partial t^2\right|_{t=0} + \partial^2 \left.\frac{\left[y_T(t)^2 + z_T(t)^2\right]}{4R_T(t)^3}/\partial t^2\right|_{t=0} \tag{40a}$$

$$Q_1 = \partial^2 \left.\frac{-y_R(t)x_R(t)}{2R_R(t)^3}/\partial t^2\right|_{t=0} + \partial^2 \left.\frac{-y_T(t)x_T(t)}{2R_T(t)^3}/\partial t^2\right|_{t=0} \tag{40b}$$

$$Q_2 = \partial^2 \left.\frac{x_R(t)^2 + z_R(t)^2}{4R_R(t)^3}/\partial t^2\right|_{t=0} + \partial^2 \left.\frac{x_T(t)^2 + z_T(t)^2}{4R_T(t)^3}/\partial t^2\right|_{t=0} \tag{40c}$$

$$T_0 = \partial^2 \left.\frac{x_R(t)\left[y_R(t)^2 + z_R(t)^2\right]}{4R_R(t)^5}/\partial t^2\right|_{t=0} + \partial^2 \left.\frac{x_T(t)\left[y_T(t)^2 + z_T(t)^2\right]}{4R_T(t)^5}/\partial t^2\right|_{t=0} \tag{40d}$$

$$T_1 = \partial^2 \left.\frac{-y_R(t)\left[2x_R(t)^2 - y_R(t)^2 - z_R(t)^2\right]}{4R_R(t)^5}/\partial t^2\right|_{t=0} + \partial^2 \left.\frac{-y_T(t)\left[2x_T(t)^2 - y_T(t)^2 - z_T(t)^2\right]}{4R_T(t)^5}/\partial t^2\right|_{t=0} \tag{40e}$$

$$T_2 = \partial^2 \left.\frac{-x_R(t)\left[x_R(t)^2 - 2y_R(t)^2 + z_R(t)^2\right]}{4R_R(t)^5}/\partial t^2\right|_{t=0} + \partial^2 \left.\frac{-x_T(t)\left[x_T(t)^2 - 2y_T(t)^2 + z_T(t)^2\right]}{4R_T(t)^5}/\partial t^2\right|_{t=0} \tag{40f}$$

$$T_3 = \partial^2 \left.\frac{y_R(t)\left[x_R(t)^2 + z_R(t)^2\right]}{4R_R(t)^5}/\partial t^2\right|_{t=0} + \partial^2 \left.\frac{y_T(t)\left[x_T(t)^2 + z_T(t)^2\right]}{4R_T(t)^5}/\partial t^2\right|_{t=0} \tag{40g}$$

REFERENCES

[1] J. Ender *et al.*, "Bistatic exploration using spaceborne and airborne SAR sensors: A close collaboration between FGAN, ZESS, and FOMAAS," in *Proc. IEEE Int. Symp. Geosci. Remote Sens.*, Jul. 2006, pp. 1828–1831.

[2] P. Dubois-Fernandez *et al.*, ''ONERA-DLR Bistatic SAR campaign: Planning, data acquistiton, and first analysis of Bistatic scattering behaviour of natural and urban targets," *IEE Proc. - Radar, Sonar Navigat.*, vol. 153, no. 3, pp. 214–223, Jun. 2006.

[3] S. V. Baumgartner *et al.*, "Bistatic experiment using TerraSAR-X and DLR's new F-SAR system," in *Proc. 7th Euro. Conf. Synthetic Aperture Radar*, Jun. 2008, pp. 1–4.

[4] I. Walterscheid *et al.*, "Bistatic SAR experiments with PAMIR and TerraSAR-X—Setup processing, and image results," *IEEE Trans. Geosci. Remote Sens.*, vol. 48, no. 8, pp. 3268–3279, Aug. 2010.

[5] H. Breit *et al.*, "Bistatic synchronization and processing of TanDEM-X data," in *Proc. IEEE Int. Geosci. Remote Sens. Symp.*, Jul. 2011, pp. 2424–2427.

[6] Y. L. Neo, F. H. Wong, and I. G. Cumming, "Processing of azimuth-invariant Bistatic SAR data using the range doppler algorithm," *IEEE Trans. Geosci. Remote Sens.*, vol. 46, no. 1, pp. 14–21, Jan. 2008.

[7] J. Wu, Z. Li, Y. Huang, J. Yang, and Q. H. Liu, "A generalized Omega-k algorithm to process translationally variant Bistatic-SAR data based on two-dimensional Stolt mapping," *IEEE Trans. Geosci. Remote Sens.*, vol. 52, no. 10, pp. 6597–6614, Oct. 2014.

[8] Z. Li, J. Wu, Y. Huang, Z. Sun, and J. Yang, "Ground-moving target imaging and velocity estimation based on mismatched compression for Bistatic forward-looking SAR," *IEEE Trans. Geosci. Remote Sens.*, vol. 54, no. 6, pp. 3277–3291, Jun. 2016.

[9] J. Wu, Z. Sun, Z. Li, Y. Huang, J. Yang, and Z. Liu, "Focusing translational variant Bistatic forward-looking SAR using keystone transform and extended nonlinear chirp scaling," *Remote Sens.*, vol. 8, no. 10, 2016, Art. no. 840.

[10] J. Wu, Z. Sun, H. An, J. Qu, and J. Yang, "Azimuth signal multichannel reconstruction and channel configuration design for geosynchronous spaceborne-airborne Bistatic SAR," *IEEE Trans. Geosci. Remote Sens.*, vol. 57, no. 4, pp. 1861–1872, Apr. 2019.

[11] J. Wu, J. Yang, Y. Huang, H. Yang, and H. Wang, "Bistatic forward-looking SAR: Theory and challenges," in *Proc. IEEE Radar Conf.*, May 2009, pp. 1–4.

[12] I. Walterscheid, T. Espeter, J. Klare, A. R. Brenner, and J. H. G. Ender, "Potential and limitations of forward-looking Bistatic SAR," in *Proc. IEEE Int. Geosci. Remote Sens. Symp.*, Jul. 2010, pp. 216–219.

[13] H. S. Shin and J. T. Lim, "Omega-k algorithm for airborne forward-looking Bistatic spotlight SAR imaging," *IEEE Geosci. Remote Sens. Lett.*, vol. 6, no. 2, pp. 312–316, Apr. 2009.

[14] Z. Li, J. Wu, W. Li, Y. Huang, and J. Yang, "One-stationary Bistatic side-looking SAR imaging algorithm based on extended keystone transforms and nonlinear chirp scaling," *IEEE Geosci. Remote Sens. Lett.*, vol. 10, no. 2, pp. 211–215, Mar. 2013.

[15] J. Wu, J. Yang, Y. Huang, H. Yang, and L. Kong, "A frequency-domain imaging algorithm for translational invariant Bistatic forward-looking SAR," *IEICE Trans. Commun.*, vol. E96.B, no. 2, pp. 605–612, Feb. 2013.

[16] J. Wu, W. Pu, Y. Huang, J. Yang, and H. Yang, "An Omega-k algorithm for Bistatic forward-looking SAR based on spectrum modeling and optimization," in *Proc. CIE Int. Conf. Radar*, Oct. 2016, pp. 1–4.

[17] W. Pu, J. Wu, X. Wang, Y. Huang, Y. Zha, and J. Yang, "Joint sparsity-based imaging and motion error estimation for BFSAR," *IEEE Trans. Geosci. Remote Sens.*, vol. 57, no. 3, pp. 1393–1408, Mar. 2019.

[18] Y. L. Neo, F. Wong, and I. G. Cumming, "A two-dimensional spectrum for Bistatic SAR processing using series reversion," *IEEE Geosci. Remote Sens. Lett.*, vol. 4, no. 1, pp. 93–96, Jan. 2007.

[19] O. Loffeld, H. Nies, V. Peters, and S. Knedlik, "Models and useful relations for Bistatic SAR processing," in *Proc. IEEE Int. Geosci. Remote Sens. Symp.*, 2003, pp. 1442–1445.

[20] R. Wang *et al.*, "A Bistatic point target reference spectrum for general Bistatic SAR processing," *IEEE Geosci. Remote Sens. Lett.*, vol. 5, no. 3, pp. 517–521, Jul. 2008.

[21] R. Wang, O. Loffeld, Y. L. Neo, H. Nies, and Z. Dai, "Extending loffeld's Bistatic formula for the general Bistatic SAR configuration," *IET Radar Sonar Navigat.*, vol. 4, no. 1, pp. 74–84, Feb. 2010.
[22] J. Wu, J. Yang, Y. Huang, Z. Liu, and H. Yang, "A new look at the point target reference spectrum for Bistatic SAR," *Progr. Electromagn. Res.*, vol. 119, no. 119, pp. 363–379, 2011.
[23] B. D. Rigling and R. L. Moses, "Polar format algorithm for Bistatic SAR," *IEEE Trans. Aerosp. Electron. Syst.*, vol. 40, no. 4, pp. 1147–1159, Oct. 2004.
[24] L. Gorham and B. Rigling, "Fast corrections for polar format algorithm with a curved flight path," *IEEE Trans. Aerosp. Electron. Syst.*, vol. 52, no. 6, pp. 2815–2824, Dec. 2016.
[25] X. Mao, D. Zhu, and Z. Zhu, "Polar format algorithm wavefront curvature compensation under arbitrary radar flight path," *IEEE Geosci. Remote Sens. Lett.*, vol. 9, no. 3, pp. 526–530, May 2012.
[26] X. Wang and D. Zhu, "Wavefront curvature correction in one stationary Bistatic SAR image focused via PFA," *Electron. Lett.*, vol. 46, no. 18, pp. 1291–1293, Sep. 2010.
[27] X. Wang, D. Zhu, X. Mao, and Z. Zhu, "Space-variant filtering for wavefront curvature correction in polar formatted Bistatic SAR image," *IEEE Trans. Aerosp. Electron. Syst.*, vol. 48, no. 2, pp. 940–950, Apr. 2012.
[28] S. Quegan, "Spotlight synthetic aperture radar: Signal processing algorithms." *J. Atmospheric Solar-Terrestrial Phys.*, vol. 59, no. 5, pp. 597–598, 1995.
[29] D. Mao and B. D. Rigling, "Distortion correction and scene size limits for SAR Bistatic polar format algorithm," in *Proc. Radar Conf.*, 2017, pp. 1103–1108.
[30] H. B. Dwight and R. H. Romer, *Tables of Integrals and Other Mathematical Data*. Basingstoke, U.K.: Macmillan, 1957.
[31] H. Deng, Y. Li, M. Liu, H. Mei, and Y. Quan, "A space-variant phase filtering imaging algorithm for missile-borne bisar with arbitrary configuration and curved track," *IEEE Sensors J.*, vol. 18, no. 8, pp. 3311–3326, Apr. 2018.

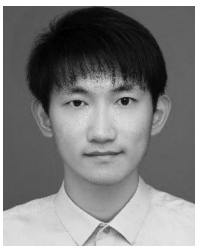

Yuxuan Miao (Student Member, IEEE) received the B.S. degree in electronic engineering from the University of Electronic Science and Technology of China (UESTC), Chengdu, China in 2016. He is currently working toward the Ph.D. degree with UESTC, Chengdu, China.

His research interests include synthetic aperture radar imaging (particular emphasis on Bistatic synthetic aperture radar).

Junjie Wu (Member, IEEE) received the B.S., M.S. and Ph.D. degrees in electronic engineering from the University of Electronic Science and Technology of China (UESTC), Chengdu, China in 2004, 2007, and 2013, respectively.

He is currently a Professor with the UESTC, Chengdu, China. From January 2012 to January 2013, he was a Visiting Student with the Department of Electrical and Computer Engineering, Duke University, Durham, NC, USA. His research interests include synthetic aperture radar imaging (particular emphasis on Bistatic synthetic aperture radar).

Mr. Wu is the Reviewer of IEEE TGRS, TSP, JSTARS, JSTSP, GRS letters, IET RSN, etc.

Zhongyu Li (Member, IEEE) received the B.S. and Ph.D. degrees in electronic engineering from the University of Electronic Science and Technology of China (UESTC), Chengdu, China, in 2011, and 2017, respectively.

From 2015 to 2016, he was a Visiting Ph.D. Student with the Department of Information Engineering, Electronics and Telecommunications, Sapienza University of Rome, Rome, Italy. He is currently an Associate Professor with UESTC. His research interest includes synthetic aperture radar technology (particular emphasis on synthetic aperture radar ground moving target detection and imaging).

Dr. Li is a Reviewer of the IEEE TRANSACTIONS ON GEOSCIENCE AND REMOTE SENSING, the IEEE GEOSCIENCE AND REMOTE SENSING LETTERS, and the *Journal of Electromagnetic Waves and Applications*.

Jianyu Yang (Member, IEEE) received the B.S. degree in electronic engineering from the National University of Defense Technology, Changsha, China, in 1984 and the M.S. and Ph.D. degrees in electronic engineering from the University of Electronic Science and Technology of China (UESTC), Chengdu, China, in 1987 and 1991, respectively.

He is currently a Professor with the School of Information and Communication Engineering, UESTC. His research interests are mainly in synthetic aperture radar (SAR) and statistical signal processing.